

PAPER

The role of adiabatic sound speeds in neutron star radial oscillations and stability

To cite this article: Sayantan Ghosh *et al* JCAP09(2025)025

View the [article online](#) for updates and enhancements.

You may also like

- [Enhancing Photovoltaic Efficiency of Quantum Dots Sensitized Solar Cell By \(001\) Oriented Anatase TiO₂ Nanosheets](#)
Kuo-Yen Huang, Yi-Hsiang Luo, Hsin-Ming Cheng et al.
- [Si/SiGe Heterointerfaces in One-, Two- and Three-Dimensional Nanostructures: Their Effect on SiGe Light Emission](#)
David J Lockwood, Xiaohua Wu, Jean-Marc Baribeau et al.
- [\(Digital Presentation\) Non-Metallic Atom \(B, C, N, O, P\) Doped-Nickel Sulfide for Efficient Electrochemical Oxygen Evolution Reaction: A First-Principles Study](#)
Xingqun Zheng and Shun Lu

RECEIVED: November 11, 2024

REVISED: May 30, 2025

ACCEPTED: July 28, 2025

PUBLISHED: September 10, 2025

The role of adiabatic sound speeds in neutron star radial oscillations and stability

Sayantani Ghosh ^{a,*} Tianqi Zhao ^{b,c} Bharat Kumar ^a
and Sailesh Ranjan Mohanty ^a

^aDepartment of Physics & Astronomy, National Institute of Technology,
Rourkela 769008, India

^bDepartment of Physics and Astronomy, Ohio University,
Athens, Ohio 45701, U.S.A.

^cUniversity of California, Berkeley,
Berkeley, CA 94720, U.S.A.

E-mail: sayantanghosh1999@gmail.com, tianqi.zhao@berkeley.edu,
kumarbh@nitrrkl.ac.in, saileshranjanmohanty@gmail.com

ABSTRACT: We investigate the impact of adiabatic sound speed on the radial oscillations and stability of neutron stars (NSs), using five representative equations of state (EOSs): three hadronic (FSU2R, HPUC, SINPA) and two hybrid (Gibbs 40, KW 55). The adiabatic case, which assumes fixed particle composition during compression, corresponds to slow reaction scenarios and leads to an extension of the stable branch toward smaller radii and higher compactness, even beyond the maximum mass configuration. This extended regime, known as the “slow stable” branch, remains dynamically stable only when reactions are sufficiently slow. To assess stability, we subject the NSs to radial perturbations and examine their fundamental radial (f -mode) oscillations, identifying the transition point where the mode frequency vanishes. The adiabatic sound speed, compared to the equilibrium sound speed, delays the onset of instability, allowing NSs to sustain stability at higher compactness and thus exhibit smaller radii — a more physically realistic outcome for slow reaction rates. Notably, the delays in the onset of instability are more pronounced for hybrid EOSs than for hadronic ones.

KEYWORDS: neutron stars, gravitational waves / theory

ARXIV EPRINT: [2401.08347](https://arxiv.org/abs/2401.08347)

*Corresponding author.

Contents

1	Introduction	1
2	Theoretical framework	4
2.1	RMF equations of state	4
2.2	Equations of state with and without quarks	5
2.3	Sound speed	9
3	Radial oscillation	12
3.1	Hydrostatic equilibrium	12
3.2	Radial oscillation equations	13
3.3	Eigenvalue problem	15
3.4	Numerical method	15
4	Results and discussion	15
5	Summary & conclusions	18
A	Radial oscillation profile	19
B	Numerical results verification	20

1 Introduction

Neutron stars (NSs), the remnants of massive stellar cores, serve as unique laboratories for nuclear physics due to their extremely dense matter. Quasi-normal modes (QNMs), which are a type of pulsation, offer critical insights into the internal composition of these stars, with pressure being the primary restoring force [1–5]. Studying these oscillations helps probe the equation of state (EOS) of dense nuclear matter, which is essential for understanding NS behaviour. Although radial oscillations themselves do not directly emit gravitational waves (GWs), they can interact with non-radial oscillation modes due to non-linear coupling, leaving imprints in the GW spectra [6, 7]. Moreover, radial oscillations can modulate the emission of short gamma-ray bursts (SGRBs) during the formation of hyper-massive neutron stars in binary NS mergers [8–11], influencing the observed properties of these events [12]. In this paper, we highlight the importance of f -mode frequency in determining the critical stable configuration of NSs, which is particularly relevant for X-ray observations of massive pulsars, such as PSR J0348+0432 with $M = 2.01 \pm 0.04 M_\odot$ [13], and PSR J0740+6620 with $M = 2.08 \pm 0.07 M_\odot$ [14–16]. Motivated by the need to refine NS models for such observations, this study examines the role of adiabatic sound speeds in radial oscillations and stability, aiming to better understand how slow reaction rates affect NS configurations and their stability limits, potentially impacting radius measurements and EOS constraints. In the adiabatic scenario, when chemical composition is considered, neutron stars with compactness exceeding that of the maximum mass configuration can exist.

The Sturm-Liouville problem concerning the linear radial oscillations of variable stars under Newtonian gravity was thoroughly investigated by Ledoux and Walraven in 1958 [17].

When the square of the eigenfrequency in the radial oscillation equations becomes negative, the fluid displacement shows exponential growth, resulting in radial oscillation instability. Chandrasekhar [18] extended these principles to derive and solve similar radial oscillation equations in the context of general relativity. The critical stable configuration in general relativity has been shown to always become unstable at a compactness $GM/(Rc^2)$ less than the Schwarzschild limit $GM/(Rc^2) = 0.5$, making it particularly relevant for compact objects like white dwarfs (WDs) and NSs.

Conversely, Harrison et al. proposed another stability criterion based on the mass-radius diagram, determined by solving the TOV equations [19]. They argued that when the total mass decreases with increasing the central density, e.g., between stable branches of WDs and NSs, the star is no longer stable under self-gravity, leading to a collapse [19]. Remarkably, for barotropic monotonic EOSs, Chandrasekhar’s and Wheeler’s methods of determining stellar instability criteria were found to be equivalent [20].

Zero-temperature NSs are often described using a barotropic EOS, where thermal effects are neglected, and the chemical composition is determined solely by beta equilibrium, which is a rapid process driven by weak interactions. This approximation is valid when the time required for beta equilibrium is much shorter than the time scale of NS oscillations, ensuring that the composition of the star remains stable during compression and expansion. However, this assumption fails when the temperature is below 1 MeV. At such low temperatures, the process of neutrino emission becomes slower than the oscillation periods of the star, preventing the star from achieving beta equilibrium during oscillations. This situation is akin to trying to synchronize a metronome with a much slower rhythm — when the tempo changes too fast, synchronization breaks down. Consequently, the matter composition remains “frozen” during oscillations, leading to a higher adiabatic index and a non-barotropic EOS. This adiabatic scenario differs from the equilibrium case in terms of sound speed: the equilibrium sound speed, defined as $c_{\text{eq}}^2 = dP/d\mathcal{E}$, assumes the composition adjusts instantaneously to perturbations, while the adiabatic sound speed, $c_{\text{ad}}^2 = (\partial P/\partial n_B)_{y_i} (\partial \mathcal{E}/\partial n_B)_{y_i}^{-1}$, accounts for fixed composition $y_i = n_i/n_B$, typically resulting in a higher value due to the stiffer response of the frozen composition. This effect extends the range of maximally stable configurations for white dwarfs (WDs), from a central density of $\rho_c = 1.2 \times 10^9 \text{ g/cm}^3$ to $\rho_c = 4 \times 10^{10} \text{ g/cm}^3$, which corresponds to the highest mass a WD can sustain before collapse [21].

The impact of this “slow weak process” varies between WDs and NSs due to differences in their beta-equilibrium compositions. For instance, the proton fraction in a WD ranges from approximately 0.5 on its surface to around 0.05 in the transition from crust to core. In contrast, the core of an NS might have a significantly different proton fraction, sometimes exceeding 0.2 [22]. Think of this as comparing the composition of different layers of a cake; the ingredients at the surface (or outer layers) might differ from those in the core. By examining how slow weak processes affect the adiabatic index, we can better understand the proton fraction, Y_e , and distinguish between different EOS models. This is akin to using a more detailed recipe to understand the nuances of a cake’s texture, helping to “break the degeneracy” of simpler barotropic EOS models [23].

When a phase transition occurs within a NS, the adiabatic index can differ markedly between catalyzed matter and matter with a fixed chemical composition [24]. Depending on the nature of the phase transition, the EOS may vary smoothly in crossover transition,

or exhibit continuity in pressure under a Gibbs construction, which describes a first-order transition with global charge neutrality and coexisting phases in equilibrium, while allowing for a discontinuity in the local baryon density or energy density of each phase. However, the total baryon density and energy density, averaged over the mixed phase, change smoothly, ensuring the EOS remains continuous on a macroscopic scale. First-order transition can also appear as a density discontinuity under Maxwell construction, where local charge neutrality is imposed. In general, the actual first-order transition may lie between these two limiting cases, depending on the surface tension and the microscopic treatment of charge screening and finite-size effects [25]. Under Maxwell construction, the transition between hadronic matter and quark matter introduces a density discontinuity that can be manifested through slow and rapid junction conditions [26], as well as intermediate junction conditions [26–28]. Although barotropic EOSs are employed for both hadronic and quark matter, they result in two distinct compositions with an infinite composition gradient [25]. This steep gradient supports non-radial g-mode oscillations, which may become detectable with advanced gravitational wave observations [29]. For radial oscillations, a significant density discontinuity combined with slow junction conditions produces a long branch of slow-stable hybrid stars [30, 31], whereas multiple density discontinuities lead to several slow-stable branches [27, 28, 32].

This work is the first to explore slow-stable NSs (both hadronic and hybrid) without density discontinuities, solving radial oscillations under the assumption of a fixed chemical composition in the slow transition limit. Previous research on non-equilibrium (adiabatic) radial oscillations has primarily focused on hadronic NSs [21, 33] or hybrid NSs with one or more density discontinuities [27, 28, 30, 31, 34, 35]. Other studies, such as those by Sen et al. [36], Routaray et al. [37], and Mohanty et al. [38], investigated radial oscillations considering various factors including quarkyonic matter, dark matter, and anisotropy, respectively. However, these works used equilibrium sound speeds for calculating radial oscillation frequencies, without accounting for composition-dependent sound speeds.

In this paper, we employ hadronic NS EOSs (FSU2R [39], HPUC [40], and SINPA [41]) and vMIT [42, 43] hybrid NS EOSs with Gibbs [29, 44, 45] or crossover constructions [46, 47]. At low and intermediate energies, these EOSs are comparable since quark contributions are negligible for FSU2R, HPUC, and SINPA, and very small for crossover models. We specifically use Gibbs and crossover EOSs with certain symmetry energy slope values (L) to avoid overlap in the mass-radius curves, selecting KW 55 and Gibbs 40 for this purpose [29]. All EOSs considered are consistent with current observational constraints on the maximum mass of NSs, approximately $2 M_{\odot}$.

This paper is organized as follows: in section 2, we outline the theoretical formalism, including detailed discussions on the RMF equations of state (subsection 2.1), the equations of state incorporating quarks (subsection 2.2), and sound speed considerations (subsection 2.3). Section 3 delves into the analysis of radial oscillations. Section 4 presents our results and their discussion. Finally, section 5 provides our conclusions. The appendix A includes the radial oscillation profiles for all five EOS models, and in appendix B we have represented the numerical verifications of our results with an independent work.

Throughout this paper, we use the mostly positive signature $(-, +, +, +)$ and employ a geometrized unit system where $G = c = \hbar = 1$.

2 Theoretical framework

2.1 RMF equations of state

The Relativistic Mean Field (RMF) model plays a crucial role in studying NS properties by providing a relativistic framework to describe the dense nuclear matter found in NSs. This model incorporates meson fields — such as sigma (σ), omega (ω), and rho (ρ) mesons — and their interactions with nucleons to formulate the EOS for nuclear matter under extreme densities and pressures. The RMF model's self-consistent mean field treatment, combined with its ability to account for relativistic effects and spin-orbit coupling, makes it a powerful tool for understanding NS properties. Despite its strengths, the RMF theory faces renormalization challenges when considering fundamental quantum chromodynamics (QCD) symmetries. These challenges are addressed by the Effective Relativistic Mean Field (E-RMF) formalism, which builds on the RMF model using effective field theory [48–56]. The E-RMF Lagrangian includes fourth-order interactions among mesons such as σ , ω , and ρ , and considers $npe\mu$ matter, as detailed in the works of [50, 52, 53, 57, 58]:

$$\begin{aligned} \mathcal{L} = & \sum_{N=p,n} \bar{\psi}_N \left\{ \gamma_\mu \left(i\partial^\mu - g_{\omega N} \omega^\mu - \frac{1}{2} g_{\rho N} \vec{\tau}_N \cdot \vec{\rho}^\mu \right) - \left(m_N - g_{\sigma N} \sigma \right) \right\} \psi_N + \sum_{l=e,\mu} \bar{\psi}_l (i\gamma_\mu \partial^\mu - m_l) \psi_l \\ & + \frac{1}{2} \partial^\mu \sigma \partial_\mu \sigma - \frac{1}{2} m_\sigma^2 \sigma^2 + \frac{\zeta}{4!} g_{\omega N}^4 (\omega^\mu \omega_\mu)^2 - \frac{\kappa}{3!} g_{\sigma N}^3 \sigma^3 - \frac{\lambda}{4!} g_{\sigma N}^4 \sigma^4 + \frac{1}{2} m_\omega^2 \omega^\mu \omega_\mu - \frac{1}{4} W^{\mu\nu} W_{\mu\nu} \\ & + \frac{1}{2} m_\rho^2 (\vec{\rho}^\mu \cdot \vec{\rho}_\mu) - \frac{1}{4} \vec{R}^{\mu\nu} \cdot \vec{R}_{\mu\nu} - \Lambda_\omega g_{\omega N}^2 g_{\rho N}^2 (\omega^\mu \omega_\mu) (\vec{\rho}^\mu \cdot \vec{\rho}_\mu). \end{aligned} \quad (2.1)$$

Here, the relevant coupling constants in the RMF model are $g_{\sigma N}$, $g_{\omega N}$, and $g_{\rho N}$, with the corresponding masses for the σ , ω , and ρ mesons denoted as m_σ , m_ω , and m_ρ , respectively. The masses of the nucleon and lepton are represented by m_N and m_l , respectively. Once the Lagrangian (\mathcal{L}) is established, the energy-momentum tensor can be derived to calculate the energy density and pressure of the system. Specifically, the energy-momentum tensor is given by [59],

$$T^{\mu\nu} = \sum_\alpha \frac{\partial \mathcal{L}}{\partial (\partial_\mu \phi_\alpha)} \partial^\nu \phi_\alpha - g^{\mu\nu} \mathcal{L}, \quad (2.2)$$

where, ϕ_α represents different fields and $g^{\mu\nu}$ is the metric tensor. The time component of the energy-momentum tensor (T^{00}) provides the total energy density, and its spatial component (T^{jj}) gives the pressure of the system as [52, 53, 55, 60],

$$\begin{aligned} \mathcal{E} = & \langle T^{00} \rangle \\ = & \frac{1}{8\pi^3} \left[\sum_{N=p,n} \gamma_N \int_0^{k_N} d^3k E_N^*(k_N) + \sum_{l=e,\mu} \gamma_l \int_0^{k_l} d^3k E_l^*(k_l) \right] \\ & + \frac{1}{2} m_\omega^2 \omega^2 + \frac{1}{2} m_\rho^2 \rho^2 + \frac{1}{2} m_\sigma^2 \sigma^2 + \frac{\kappa}{3!} (g_{\sigma N} \sigma)^3 \\ & + \frac{\lambda}{4!} (g_{\sigma N} \sigma)^4 + \frac{\zeta}{8} (g_{\omega N} \omega)^4 + 3\Lambda_\omega g_{\omega N}^2 g_{\rho N}^2 \omega^2 \rho^2, \end{aligned} \quad (2.3)$$

$$\begin{aligned}
 P &= \frac{1}{3} \langle T^{jj} \rangle \\
 &= \frac{1}{24\pi^3} \left[\sum_{N=p,n} \gamma_N \int_0^{k_N} d^3k \frac{k^2}{E_N^*(k_N)} + \sum_{l=e,\mu} \gamma_l \int_0^{k_l} d^3k \frac{k^2}{E_l(k_l)} \right] \\
 &\quad + \frac{1}{2} m_\omega^2 \omega^2 + \frac{1}{2} m_\rho^2 \rho^2 - \frac{1}{2} m_\sigma^2 \sigma^2 - \frac{\kappa}{3!} (g_{\sigma N} \sigma)^3 \\
 &\quad - \frac{\lambda}{4!} (g_{\sigma N} \sigma)^4 + \frac{\zeta}{24} (g_{\omega N} \omega)^4 + \Lambda_\omega g_{\omega N}^2 g_{\rho N}^2 \omega^2 \rho^2.
 \end{aligned} \tag{2.4}$$

The energy density for leptons and nucleons in the meson medium is given by $E_l(k_l) = \sqrt{k_l^2 + m_l^2}$ and $E_N^*(k_N) = \sqrt{k_N^2 + m_N^{*2}}$, respectively. Here, m_N^* represents the effective mass of the nucleon, and k_N denotes its momentum, where N refers to protons (p) or neutrons (n). For leptons, m_l is the mass, and k_l is the momentum, with l indicating electrons (e) or muons (μ). The spin degeneracy factor γ_N is 2 for each type of nucleon. By utilizing these energy densities and pressures, one can derive various properties of finite nuclei, nuclear matter, and neutron stars. In this work, we employ three different parameter sets: FSU2R [39], HPUC [40], and SINPA [41]. Table 1 provides the coupling constants and empirical values related to nuclear matter properties at saturation for these parameter sets.

To solve for neutron star matter and determine the particle fractions as functions of baryon density for the FSU2R, HPUC, and SINPA models, we first derived the Euler-Lagrange equations of motion for the mesons from the Lagrangian. We then applied the constraints of baryon number conservation and charge neutrality:

$$n_B = \sum_N n_N \quad (N \in \text{nucleons}) \tag{2.5}$$

$$0 = \sum_K q_K n_K \quad (K \in \text{nucleons, leptons}). \tag{2.6}$$

Additionally, we imposed chemical equilibrium with respect to weak processes, as detailed in [61].

2.2 Equations of state with and without quarks

2.2.1 Quark matter EOS

The vMIT bag model [42, 43] has been used here to calculate the quark EOS, whose Lagrangian density is given by

$$\mathcal{L} = \sum_{q=u,d,s} \left[\bar{\psi}_q (i\gamma\partial - m_q) \psi_q - B + \mathcal{L}_{\text{vec}} \right] \Theta. \tag{2.7}$$

\mathcal{L}_{vec} defined as,

$$\mathcal{L}_{\text{vec}} = -G_v \sum_q \bar{\psi} \gamma_\mu V^\mu \psi + \left(m_V^2/2 \right) V_\mu V^\mu. \tag{2.8}$$

The notations used here and the values adopted are taken from [29]. The corresponding expressions for energy density, chemical potentials, and pressure, derived from the given

	FSU2R	HPUC	SINPA	Emp/Expt	Unit
m_σ	497.479	506.460	495.394	-	MeV
m_ω	782.5	782.5	782.5	-	MeV
m_ρ	763.0	763.0	763.0	-	MeV
$g_{\sigma N}^2$	107.57	107.68	112.97	-	-
$g_{\omega N}^2$	182.39	172.70	191.91	-	-
$g_{\rho N}^2$	247.34	231.71	164.63	-	-
κ	3.0911	4.3627	3.556	-	MeV
λ	-0.001680	-0.00428	-0.00293	-	-
ζ	0.024	0.0230202	0.0279	-	-
Λ_ω	0.05	0.061275	0.038279	-	-
n_0	0.1505	0.149	0.151	0.148–0.185 ^(a)	fm^{-3}
E/A	-16.28	-15.98	-16.00	(-15)–(-17) ^(a)	MeV
K	238.00	220.20	203.00	220–260 ^(b)	MeV
$E_{\text{sym}}(n_0)$	30.20	28.40	31.20	30.20–33.70 ^(c)	MeV
L	44.30	41.60	53.86	35.00–70.00 ^(c)	MeV

Table 1. Parameters of the model FSU2R [39], HPUC [40] and SINPA [41]. The mass of the nucleon, $m_N = 939$ MeV and the mass of the muon, $m_\mu = 105.7$ MeV. In the lower panel, we report the values of saturation density (n_0), energy per nucleon (E/A), the incompressibility (K) of symmetric nuclear matter, symmetry energy (E_{sym}) at n_0 and the slope parameter of the symmetry energy (L). For reference, empirical or experimental estimates, along with citations, are listed in the second last column as (a) [62], (b) [63], (c) [64].

Lagrangian prior to imposing baryon number conservation, charge neutrality, and chemical equilibrium, are as follows:

$$\varepsilon_Q = \sum_{q=u,d,s} \varepsilon_q + \frac{1}{2} a [n_B(y_u + y_d + y_s)]^2 + B \quad (2.9)$$

$$\varepsilon_q = \frac{3}{8\pi^2} \left\{ k_{Fq} (k_{Fq}^2 + m_q^2)^{1/2} (2k_{Fq}^2 + m_q^2) - m_q^4 \ln \left[\frac{k_{Fq} + (k_{Fq}^2 + m_q^2)^{1/2}}{m_q} \right] \right\} \quad (2.10)$$

$$\mu_q = (k_{Fq}^2 + m_q^2)^{1/2} + a n_B (y_u + y_d + y_s) \quad (2.11)$$

$$p_Q = n_B \sum_{q=u,d,s} \mu_q y_q - \varepsilon_Q \quad (2.12)$$

where $a \equiv (G_v/m_V)^2$ and $k_{Fq} = (\pi^2 n_B y_q)^{1/3}$. We fix the vector interaction parameter $a = 0.2 \text{ fm}^2$ and the bag constant $B^{1/4} = 180 \text{ MeV}$.

2.2.2 Leptons

Due to the relatively small value of the electromagnetic fine-structure constant, $\alpha \simeq 1/137$, leptons can be effectively modelled as non-interacting, relativistic particles. Consequently,

$$\varepsilon_L = \frac{3}{8\pi^2\hbar^3} \left\{ k_{Fl}(k_{Fl}^2 + m_l^2)^{1/2}(2k_{Fl}^2 + m_l^2) - m_l^4 \ln \left[\frac{k_{Fl} + (k_{Fl}^2 + m_l^2)^{1/2}}{m_l} \right] \right\} \quad (2.13)$$

$$p_L = \sum_{l=e,\mu} n_l \mu_l - \varepsilon_L \quad (2.14)$$

where $\mu_l = (k_{Fl}^2 + m_l^2)^{1/2}$ and $k_{Fl} = (3\pi^2 n_l)^{1/3}$ for $l = e, \mu$. At low baryon number densities, the system contains only electrons. Muons begin to populate the system once the baryon density n_B reaches a value where the condition $\mu_e = m_\mu$ is satisfied.

2.2.3 Crossover matter

To evaluate the properties of crossover matter, we adopt the Kapusta-Welle (KW) framework [46, 47], within which the pressure is formulated as follows,

$$p_B = (1 - S)p_H + S p_Q. \quad (2.15)$$

Here, p_H and p_Q represent the pressures in the pure hadronic and quark phases, respectively. The switching function controls the smooth transition between these two phases, defined as,

$$S = \exp \left[- \left(\frac{\mu_0}{\mu} \right)^4 \right] \quad (2.16)$$

where μ is the average nucleonic chemical potential

$$\mu = \frac{n_n \mu_n + n_p \mu_p}{n_n + n_p} \quad (2.17)$$

where μ_0 denotes a characteristic energy scale associated with the crossover, set to $\mu_0 = 1.8 \text{ GeV}$ in this context. By applying the grand-canonical relation $n_i = \frac{\partial p}{\partial \mu_i} \Big|_{\mu_j}$ to eq. (2.15), we obtain,

$$n_h^* = n_h \left[1 - S \left(1 - \frac{4\mu_0^4}{\mu^5} \frac{p_Q - p_H}{n_n + n_p} \right) \right] \quad \text{for } h = n, p \quad (2.18)$$

$$n_q^* = S n_q \quad \text{for } q = u, d, s. \quad (2.19)$$

The starred quantities represent the densities of nucleons and quarks in the crossover matter, whereas the unstarred ones refer to their values in the pure hadronic and quark phases. The leptonic properties remain unchanged, which is unnecessary as their properties remain unaffected. The baryonic energy density ε_B is expressed as,

$$\varepsilon_B = -p_B + \sum_{i=n,p,u,d,s} n_i^* \mu_i. \quad (2.20)$$

The chemical potentials in crossover matter are (functionally) the same as in the pure phases.

To accurately model hybrid NS matter, composed of nucleons, leptons, and quarks, the initially unconstrained system must be constrained by the conditions imposed by strong

$$\mu_n = 2\mu_d + \mu_u; \quad \mu_p = 2\mu_u + \mu_d \quad (2.21)$$

and weak equilibrium

$$\mu_n = \mu_p + \mu_e; \quad \mu_e = \mu_\mu; \quad \mu_d = \mu_s \quad (2.22)$$

as well as to charge neutrality

$$n_p^* + (2n_u^* - n_d^* - n_s^*)/3 - (n_e + n_\mu) = 0 \quad (2.23)$$

and baryon number conservation

$$n_n^* + n_p^* + (n_u^* + n_d^* + n_s^*)/3 - n_B = 0. \quad (2.24)$$

These constraints allow the particle fractions to be expressed in terms of the total baryon density:

$$y_i \rightarrow y_{i,\beta}(n_B); \quad i = n, p, u, d, s, e, \mu \quad (2.25)$$

2.2.4 Gibbs construction

In crossover matter, thermodynamic quantities are represented as functions of the total baryon density n_B and the individual particle fractions $y_n, y_p, y_e, y_\mu, y_u, y_d$, and y_s , which are considered independent variables. The Gibbs construction [44, 45] incorporates an extra independent parameter, χ , which denotes the quark volume fraction within the mixed phase arising from a soft first-order phase transition. This relationship is given by:

$$\varepsilon_B = (1 - \chi)\varepsilon_H + \chi\varepsilon_Q; \quad (2.26)$$

that is, the mixed phase is defined by the condition $0 \leq \chi \leq 1$.

Afterwards, the conditions for mechanical, strong, and weak equilibrium, charge neutrality, and baryon number conservation are applied:

$$p_H = p_Q; \quad \mu_n = 2\mu_d + \mu_u; \quad \mu_p = 2\mu_u + \mu_d \quad (2.27)$$

$$\mu_n = \mu_p + \mu_e; \quad \mu_e = \mu_\mu; \quad \mu_d = \mu_s \quad (2.28)$$

$$3(1 - \chi)y_p + \chi(2y_u - y_d - y_s) - 3(y_e + y_\mu) = 0 \quad (2.29)$$

$$3(1 - \chi)(y_n + y_p) + \chi(y_u + y_d + y_s) - 3 = 0. \quad (2.30)$$

By solving these equations, the variables y_i and χ are expressed in terms of the total baryon density n_B , effectively eliminating them as independent parameters. Consequently, the state variables depend solely on n_B , following the relation:

$$Q(n_B, y_i, y_j, \dots) \rightarrow Q[n_B, y_i(n_B), y_j(n_B), \dots] = Q(n_B).$$

For the mixed (*) phase,

$$\varepsilon^* = (1 - \chi)\varepsilon_H + \chi\varepsilon_Q + \varepsilon_L \quad (2.31)$$

$$\begin{aligned} p^* &= p_H + p_L = p_Q + p_L \\ &= (1 - \chi)p_H + \chi p_Q + p_L \end{aligned} \quad (2.32)$$

$$\mu_h^* = \mu_h; \quad \mu_q^* = \mu_q \quad (2.33)$$

$$y_h^* = (1 - \chi)y_h; \quad y_q^* = \chi y_q. \quad (2.34)$$

Leptonic quantities remain unaffected by the relative proportions of the two baryonic phases within the mixed region.

2.3 Sound speed

Phase transitions or crossovers in dense matter within NSs significantly impact the speed of sound, $c_s^2(n_B)$, as a function of baryon density (n_B). Extreme conditions that alter the internal composition or structure of the matter produce distinct signatures in the propagation of sound [65–72]. The study of these variations in the speed of sound is crucial for probing different EOSs and for understanding the fundamental properties of NSs, including the presence of exotic states of matter.

In the case of RMF models, the composition of matter in the NS core is determined by the conditions of charge neutrality and beta-equilibrium. These conditions ensure that the system is in weak interaction equilibrium and are expressed as:

$$\mu_n = \mu_p + \mu_e, \quad (2.35)$$

$$\mu_e = \mu_\mu, \quad (2.36)$$

where μ_n , μ_p , μ_e , and μ_μ are the chemical potentials of neutrons, protons, electrons, and muons, respectively. These relations guarantee equilibrium among the various species of fermions. For each value of baryon density n_B , we solve these equations self-consistently to determine the particle fractions and compute the corresponding total pressure $P(n_B)$ and energy density $\mathcal{E}(n_B)$. These quantities are then used to compute the sound speed.

The equilibrium speed of sound is computed using the thermodynamic relation:

$$c_{\text{eq}}^2 = \frac{dP}{d\mathcal{E}}, \quad (2.37)$$

where P is the pressure and \mathcal{E} is the total energy density. For cold neutron star matter, where the entropy per baryon is negligible, this derivative is taken at constant entropy.

In practice, for tabulated EOSs, we approximate this derivative numerically via finite differences:

$$c_{\text{eq},k}^2 \approx \frac{\Delta P}{\Delta \mathcal{E}} = \frac{P_{k+1} - P_k}{\mathcal{E}_{k+1} - \mathcal{E}_k}, \quad (2.38)$$

the subscript k here denotes the k^{th} point in the tabulated EOS data. This computation is implemented using numerical routines such as `numpy.gradient` in Python, which accurately estimates the derivative even for non-uniformly spaced data points. We also ensure the causality condition $c_{\text{eq}}^2 \leq c^2$ is satisfied (see figure 2).

In contrast, the adiabatic sound speed cannot be calculated directly from the EOS alone. To determine it, we need to account for the specific composition of the matter described by the EOS, such as npe (neutrons, protons, electrons), $npe\mu$ (neutrons, protons, electrons, muons), or quark (uds) matter. The adiabatic sound speed is expressed as:

$$c_{\text{ad}}^2 = \left(\frac{\partial P}{\partial n_B} \right)_{y_i} \left(\frac{\partial \mathcal{E}}{\partial n_B} \right)_{y_i}^{-1}, \quad (2.39)$$

where y_i represents the particle fraction relative to the total baryon number density (n_B). This expression indicates that calculating the adiabatic sound speed requires partial differentiation of the total pressure and energy density with respect to baryon number density for a fixed composition. So for the calculation of a fixed composition around equilibrium, the second term in the right-hand side of eq. (2.39) is equivalent to,

$$\left(\frac{\partial \mathcal{E}}{\partial n_B} \right)_{y_i} = \sum_i \left(\frac{\partial \mathcal{E}}{\partial n_i} \right)_{n_{j \neq i}} \left(\frac{\partial n_i}{\partial n_B} \right)_{y_i} \quad (2.40)$$

where n_i , are the particle number density and i represents the different particles. We know from the definition of particle fraction [61],

$$y_i = \frac{n_i}{n_B} \quad (2.41)$$

or,

$$n_i = y_i n_B. \quad (2.42)$$

Now, if we put this in the 2nd term of the right hand equality of eq. (2.40), we get,

$$\left(\frac{\partial n_i}{\partial n_B} \right)_{y_i} = \left(\frac{\partial (y_i n_B)}{\partial n_B} \right)_{y_i} = y_i \left(\frac{\partial n_B}{\partial n_B} \right)_{y_i} = y_i. \quad (2.43)$$

Plugging in the definition of the chemical potential and particle fraction of each composition as in eq. (2.40),

$$\mu_i = \left(\frac{\partial \mathcal{E}}{\partial n_i} \right)_{n_{j \neq i}}, \quad y_i = \left(\frac{\partial n_i}{\partial n_B} \right)_{y_i}, \quad (2.44)$$

we can introduce the average chemical potential [24],

$$\left(\frac{\partial \mathcal{E}}{\partial n_B} \right)_{y_i} = \sum_i \mu_i y_i \equiv \mu_{\text{avg}}. \quad (2.45)$$

Using the eq. (2.40) in eq. (2.39), the adiabatic sound speed can be expressed as,

$$c_{\text{ad}}^2 = \frac{1}{\mu_{\text{avg}}} \left(\frac{\partial P}{\partial n_B} \right)_{y_i}. \quad (2.46)$$

For a fixed value of y_i (as shown in figure 1), we first calculate the average chemical potential, μ_{avg} , and the derivative $\left(\frac{\partial P}{\partial n_B} \right)_{y_i}$. Since $\left(\frac{\partial P}{\partial n_B} \right)_{y_i}$ is not analytically straightforward in RMF models due to the complexities of the meson fields, we compute this derivative numerically using the finite difference method. We then use eq. (2.39) to determine the adiabatic sound speed.

In figure 1, the variation of particle fractions ($y_i = n_i/n_B$) for neutrons, protons, electrons, muons, and quarks as functions of baryon number density is shown for various EOSs. The appearance of muons, governed by the condition $\mu_e > m_\mu$, occurs slightly above the nuclear saturation density ($n_B \approx 0.16 \text{ fm}^{-3}$). In the upper panel for nucleonic EOSs, particles appear

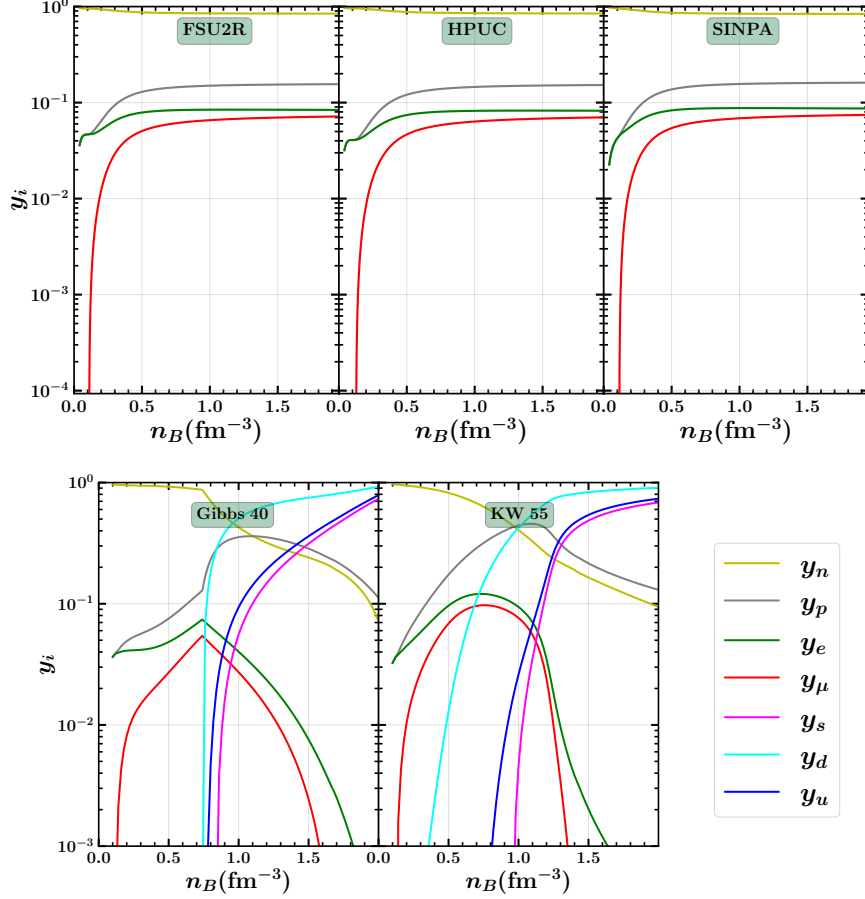


Figure 1. Particle fractions ($y_i = n_i/n_B$) as a function of total baryon number density (n_B). Where $i = n, p, e, \mu, s, d, u$ represents neutron, proton, electron, muon, strange quark, down quark and up quark respectively.

and persist as the baryon density varies. Whereas, the lower panel for Gibbs 40 and KW 55 shows that n, p, e , and μ appear initially but vanish beyond a certain baryon density, where quarks begin to dominate and continue to vary with the baryon density. The figure illustrates smooth transitions in particle composition for nucleonic EOSs in the upper panel, while the KW model demonstrates continuous profiles in the lower right panel. In contrast, the Gibbs model in the lower left panel reveals a gradual yet uneven transition to quark matter, introducing subtle shifts in the quark ratio rather than abrupt changes. This unevenness impacts the equilibrium sound speed, leading to discontinuities.

Figure 2 highlights the resulting sound speed variations and their connection to the composition. In the left panel, equilibrium and adiabatic sound speeds (c_s^2) are plotted as functions of baryon density (n_B). For $npe\mu$ matter in models such as FSU2R, HPUC, and SINPA, the equilibrium sound speed increases consistently with rising baryon density. However, the inclusion of quarks in the KW 55 and Gibbs 40 models alters this behavior. The KW model exhibits a smoother and more gradual increase in equilibrium sound speed, reflecting the continuous composition gradient shown in figure 1. By contrast, the Gibbs model displays a sharp discontinuity due to the uneven transition to quark matter, which

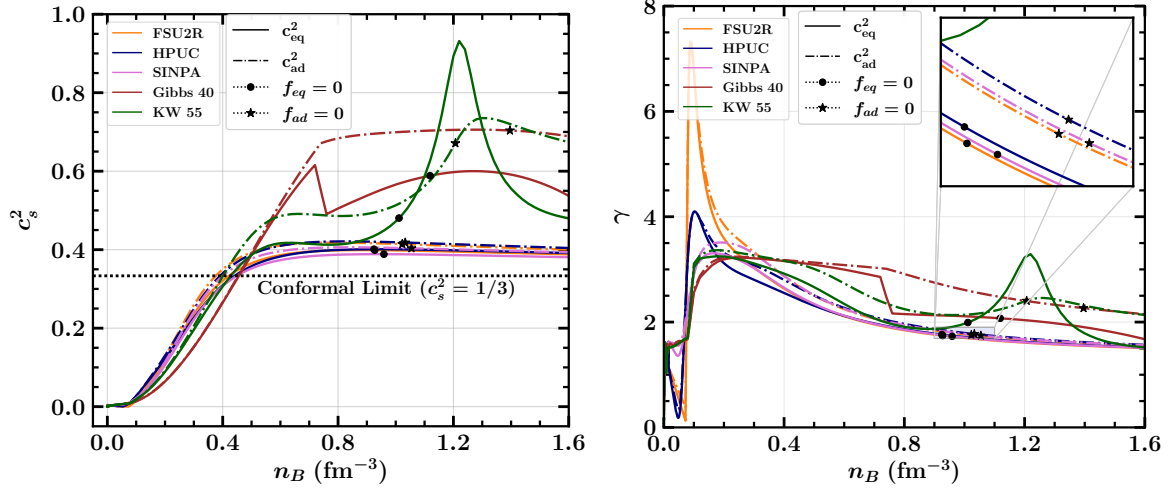


Figure 2. On the left panel, the squared sound speeds (c_s^2) are presented as functions of baryon number density (n_B), delineating the relationship between the local speed of sound and the density of baryonic matter. The right panel exhibits the adiabatic index (γ) as a function of baryon number density (n_B) for the specified models detailed in the inset. Solid lines represent the equilibrium case, while dashed-dot lines depict the adiabatic scenario. The horizontal dotted line represents the conformal limit ($c_s^2 = 1/3$) of sound speed. The star and dot marker are the points where f -mode frequency for adiabatic (f_{ad}) and equilibrium (f_{eq}) cases respectively become zero. The “zoomed plot” clearly shows the different markers on the variation of γ for RMF EOSs.

disrupts the monotonic growth of c_s^2 . The adiabatic sound speed, calculated under fixed composition conditions, also remains continuous for both KW and Gibbs models, as their individual sound speed components are continuous. The right panel of figure 2 illustrates the adiabatic index (γ), where similar trends are observed. The smoother variation of the adiabatic sound speed in the KW model translates into a less abrupt change in γ , while the discontinuities in the Gibbs model produce more pronounced deviations. The effects of quark content are evident in both the sound speed and adiabatic index, with the distinct behavior of the KW and Gibbs models highlighting differences in phase transition characteristics.

3 Radial oscillation

NSs achieve very high densities and energies, thus requiring general relativistic effects. We derive radial oscillations of NSs in a relativistic framework, assuming a non-rotating, spherically symmetric NS in hydrostatic and thermal equilibrium when unperturbed. The oscillations are harmonic and adiabatic, with no net heat exchange and small enough for linear theory to apply [73].

3.1 Hydrostatic equilibrium

For the conditions mentioned above, the spacetime metric can be expressed as,

$$ds^2 = -e^{2\nu} dt^2 + e^{2\lambda} dr^2 + r^2(d\theta^2 + \sin^2\theta d\phi^2), \quad (3.1)$$

where $\lambda \equiv \lambda(r)$ and $\nu \equiv \nu(r)$ are metric functions, each following their respective set of equations. Here, the energy-momentum tensor $T_{\mu\nu}$ takes the form of a perfect fluid:

$$T_{\mu\nu} = (P + \mathcal{E})u_\mu u_\nu + P g_{\mu\nu}, \quad (3.2)$$

where P is pressure, \mathcal{E} is energy density, $g_{\mu\nu}$ is the metric tensor and u_μ represents covariant velocity. In spherical symmetry, the component u_0 exhibits non-zero values along the radial direction (however if we add the perturbation u_0 and u_1 both exhibit non-zero values) and must satisfy $u_\mu u^\mu = -1$. Einstein's field equations, using natural units where $G = c = 1$, are given by:

$$G_{\mu\nu} = R_{\mu\nu} - \frac{1}{2}R g_{\mu\nu} = \kappa T_{\mu\nu}, \quad (3.3)$$

where $\kappa = 8\pi$, $G_{\mu\nu}$ is the Einstein tensor, and $R_{\mu\nu}$ and R are the Ricci tensor and Ricci scalar, respectively. Applying Einstein's field equations to the Schwarzschild metric in eq. (3.1) under equilibrium conditions and utilizing the boundary condition $\lambda(r=0) = 0$, we obtain:

$$e^{-2\lambda(r)} = \left(1 - \frac{2m}{r}\right). \quad (3.4)$$

The mass m can be determined through integration using:

$$\frac{dm}{dr} = 4\pi r^2 \mathcal{E}. \quad (3.5)$$

Likewise, employing the law of conservation of momentum, we obtain [74]:

$$\frac{d\nu}{dr} = -\frac{1}{P + \mathcal{E}} \frac{dP}{dr}. \quad (3.6)$$

Ultimately, employing eq. (3.6) and Einstein's field equations leads to [75, 76]:

$$\frac{dP}{dr} = -\frac{m}{r^2} \frac{(P + \mathcal{E}) \left(1 + \frac{4\pi r^3 P}{m}\right)}{\left(1 - \frac{2m}{r}\right)}. \quad (3.7)$$

Eqs. (3.4) and (3.6) describe the behaviour of the metric functions within the NS where $r < R$. At the surface, i.e. at $r = R$, they satisfy the boundary condition,

$$e^{2\nu(R)} = e^{-2\lambda(R)} = \left(1 - \frac{2M}{R}\right). \quad (3.8)$$

Eq. (3.8) remains valid even beyond the star, where R is replaced by r for $r > R$, taking on the familiar form of the Schwarzschild solution.

3.2 Radial oscillation equations

Maintaining the spherical symmetry of the background equilibrium configuration, we introduce perturbations to both the fluid and spacetime variables. The radial displacement of a fluid element located at position r in the unperturbed model is assumed to exhibit harmonic time dependence as,

$$\delta r(r, t) = X(r) e^{i\omega t}. \quad (3.9)$$

The equations for linearized radial perturbations can be expressed as [18, 77]

$$c_s^2 X'' + \left((c_s^2)' - Z + 4\pi r \gamma P e^{2\lambda} - \nu' \right) X' + \left[2(\nu')^2 + \frac{2m}{r^3} e^{2\lambda} - Z' - 4\pi(P + \mathcal{E}) Z r e^{2\lambda} + \omega^2 e^{2\lambda-2\nu} \right] X = 0. \quad (3.10)$$

Here, primes represent differentiation with respect to the radial coordinate r , and c_s^2 denotes the square of the speed of sound. Z defined as,

$$Z(r) = c_s^2 \left(\nu' - \frac{2}{r} \right). \quad (3.11)$$

The adiabatic index, γ , is related to the speed of sound as follows:

$$\gamma = \left(\frac{P + \mathcal{E}}{P} \right) c_s^2. \quad (3.12)$$

Now we can define the γ by considering the two different kinds of sound speeds, as

$$\gamma_{\text{eq}} = \left(\frac{P + \mathcal{E}}{P} \right) c_{\text{eq}}^2, \quad (3.13)$$

$$\gamma_{\text{ad}} = \left(\frac{P + \mathcal{E}}{P} \right) c_{\text{ad}}^2, \quad (3.14)$$

where the suffix “eq” and “ad” correspond to the equilibrium and adiabatic case respectively. Now, we re-define the displacement function as

$$\zeta = r^2 e^{-\nu} X. \quad (3.15)$$

Eq. (3.10) can be rewritten for ζ as

$$\frac{d}{dr} \left(H \frac{d\zeta}{dr} \right) + (\omega^2 W + Q) \zeta = 0, \quad (3.16)$$

with

$$H = r^{-2} (P + \mathcal{E}) e^{\lambda+3\nu} c_s^2 \quad (3.17a)$$

$$W = r^{-2} (P + \mathcal{E}) e^{3\lambda+\nu} \quad (3.17b)$$

$$Q = r^{-2} (P + \mathcal{E}) e^{\lambda+3\nu} \left((\nu')^2 + \frac{4}{r} \nu' - 8\pi e^{2\lambda} P \right). \quad (3.17c)$$

H , W , and Q are dependent on the radial coordinate r and can be computed using the unperturbed background configuration. Notably, eq. (3.16) explicitly reveals its self-adjoint nature. The Lagrangian variation of the pressure now is

$$\Delta P = -r^{-2} e^\nu (P + \mathcal{E}) c_s^2 \zeta'. \quad (3.18)$$

As radial oscillations cannot displace the fluid element at the center, the boundary condition at the center is

$$X(r = 0) = 0. \quad (3.19)$$

At the stellar surface, the Lagrangian variation of pressure should vanish, expressed as

$$\Delta P(R) = 0. \quad (3.20)$$

The differential eq. (3.16), subject to the boundary conditions in eqs. (3.19) and (3.20), constitutes a Sturm-Liouville eigenvalue problem [77, 78].

3.3 Eigenvalue problem

The eigenvalues, denoted as ω_n^2 , are real and constitute an infinite, discrete sequence arranged in ascending order:

$$\omega_0^2 < \omega_1^2 < \omega_2^2 < \dots < \omega_n^2 < \dots$$

The eigenfunction corresponding to the n -th mode exhibits exactly n zero crossings between the center and the surface of the star. When ω^2 is positive, ω is real, indicating a purely oscillatory behavior. However, if ω^2 becomes negative, the frequency becomes imaginary, which corresponds to an exponentially growing solution. The general solution to the radial oscillations is a superposition of all such modes ω_n , and the presence of an exponentially growing solution indicates instability in the radial oscillations. For NSs, the fundamental mode ω_0 becomes unstable when the central density ρ_c exceeds the critical density ρ_{critical} associated with the maximum mass configuration. This instability can ultimately lead to the collapse of the star into a black hole.

3.4 Numerical method

For numerical integration [36, 37, 77, 79], we write eq. (3.16) as a system of two first-order differential equations in ζ and $\eta = H\zeta'$:

$$\frac{d\zeta}{dr} = \frac{\eta}{H} \quad (3.21)$$

and

$$\frac{d\eta}{dr} = -(\omega^2 W + Q)\zeta. \quad (3.22)$$

Expanding ζ and η close to the origin and comparing the leading order coefficients gives $\eta_0 = 3\zeta_0 H_0$ [77]. Here η_0 , ζ_0 and H_0 are their corresponding values at $r = r_{\text{min}}$, where r_{min} is the smallest radial coordinate considered in the integration of the TOV equations. Choosing $\eta_0 = 1$, we get $\zeta_0 = 1/(3H_0)$. At the surface, boundary condition eq. (3.20) implies

$$\eta(R) = 0. \quad (3.23)$$

For an arbitrary value of ω , the integration can be done from the stellar centre to its surface, where $\eta(R)$ is obtained. Those ω 's for which eq. (3.23) is satisfied, are the eigenfrequencies of the radial oscillation. Our numerical results for radial oscillations were verified against independent studies [80], see in appendix B.

4 Results and discussion

This section presents the numerical results for five EOSs — FSU2R, HPUC, SINPA (hadronic), and Gibbs 40, KW 55 (hybrid) — focusing on how adiabatic sound speeds, compared to equilibrium ones, influence NS radial oscillations and stability under slow reaction conditions. Our study examines variations in sound speed and adiabatic index, which affect NS properties such as mass and radius. We also analyze f -mode oscillations to assess the star's stability and structure, as these modes provide insights into its dynamic response to perturbations

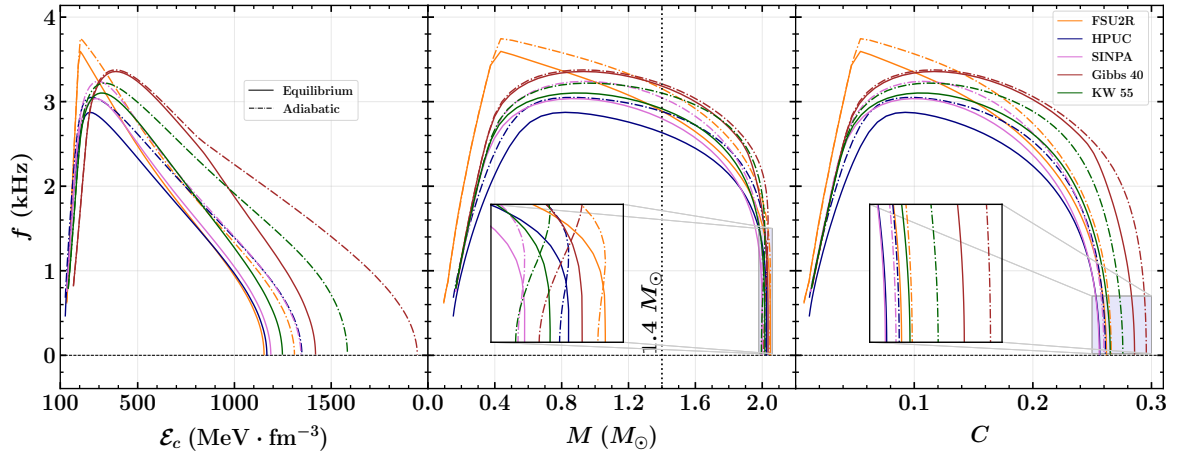


Figure 3. On the left panel, the f -mode frequency is depicted as a function of central energy density (\mathcal{E}_c), offering insights into the dynamic behaviour in response to varying internal energy conditions. The middle panel illustrates the f -mode frequency against the mass (M). In the right panel, we show the variation of f -mode with the compactness (C). The vertical dotted line in the middle panel is the line corresponding to $1.4 M_\odot$. The “zoomed plots” in the middle and right panel clearly show the variation of the adiabatic and equilibrium frequencies close to the “ $f = 0$ ” line.

and internal composition. To confirm that the calculated frequencies correspond to the fundamental f -modes, we provide a detailed analysis of radial oscillation profiles in appendix A, including the radial variation of f -modes and the first two pressure modes (p_1 and p_2) for all five EOSs. The profiles were examined by counting nodes: f -modes have no nodes, while higher-order modes like p_1 and p_2 exhibit one or more nodes, validating that the frequencies we are focusing in this study indeed correspond to the fundamental modes. To ensure the robustness of our numerical implementation, we have verified our results for sound speed, mass-radius relations, and f -mode frequencies against an independent study [80], using EOSs APR, Kulera 2014-I & II, and TM1. The comparison, which shows good agreement, is detailed in appendix B.

In figure 3, the left panel shows the f -mode frequency variation with central energy density (\mathcal{E}_c), while the middle and right panels display variations with mass (M) and compactness ($C = M/R$), respectively, to explore radial oscillations and stability. All EOSs exhibit consistent trends. The left panel indicates that for Gibbs 40 and KW 55, the central energy density exceeds that of the hadronic EOSs (FSU2R, HPUC, SINPA) in both equilibrium and adiabatic cases at a fixed frequency. This behavior reflects the higher adiabatic and equilibrium sound speeds in Gibbs 40 and KW 55, which result from their stiffer EOSs compared to the hadronic models, as shown in figure 2. Besides, the difference between solid and dashed lines arises from the timescales for reaching equilibrium: in the equilibrium case (solid lines), NS matter rapidly stabilizes, causing the f -mode frequency to vanish at a lower central density; in the adiabatic case (dashed-dot lines), the slower process extends stability, with the frequency vanishing at a higher central density. This distinction is more pronounced in hybrid models than in hadronic models, since the difference between adiabatic and equilibrium sound speeds is greater in the former, as also illustrated in figure 2.

EOS	$R_{1.4}$	$f_{1.4}^{\text{eq}}$	$f_{1.4}^{\text{ad}}$
FSU2R	12.65	2.89	3.15
HPUC	13.16	2.64	2.89
SINPA	12.90	2.81	3.05
Gibbs 40	11.73	3.18	3.21
KW 55	12.52	2.92	3.10

Table 2. NS parameters at $1.4 M_{\odot}$ for chosen EOSs. Radius in (km) and frequencies (f) are in kHz.

EOS	$f_{\text{eq}} = 0$				$f_{\text{ad}} = 0$			
	\mathcal{E}_c	M	R	C	\mathcal{E}_c	M	R	C
FSU2R	1153.51	2.05	11.54	0.262	1309.20	2.04	11.34	0.266
HPUC	1167.79	2.03	11.66	0.256	1348.21	2.02	11.42	0.261
SINPA	1187.85	2.00	11.53	0.255	1342.39	1.99	11.33	0.259
Gibbs 40	1419.05	2.04	10.52	0.285	1944.90	2.01	10.03	0.295
KW 55	1247.90	2.02	11.22	0.265	1583.96	1.99	10.67	0.275

Table 3. NS parameters at the point where f -mode frequencies vanish for both equilibrium and adiabatic cases across chosen EOSs. Central energy density (\mathcal{E}_c) is in $\text{MeV} \cdot \text{fm}^{-3}$, Mass (M) in M_{\odot} , Radius (R) in km, and Compactness (C).

The middle panel shows that near $1.4 M_{\odot}$, the f -mode frequency for Gibbs 40 exceeds that of KW 55, which in turn surpasses the hadronic EOSs (table 2). A zoomed plot in the middle panel reveals that the f -mode frequency in the equilibrium case vanishes at a higher mass than in the adiabatic case. Similarly, the right panel’s zoomed plot shows the equilibrium case frequency vanishing at lower compactness than the adiabatic case, indicating that adiabatic conditions sustain more compact NSs before instability. This effect is more pronounced for hybrid EOSs due to the additional degree of freedom from quarks, which increases the difference between adiabatic and equilibrium sound speeds, and is greater in the former as shown in figure 2. The points where the f -mode frequency vanishes are marked with dots (equilibrium) and stars (adiabatic) in the figures (table 3), where:

- The star marker indicates the adiabatic f -mode frequency reaching zero, beyond the maximum mass configuration.
- The dot marker denotes the equilibrium f -mode frequency reaching zero, typically at the maximum mass.

The left panel of figure 4 displays pressure and energy density variations for the five EOSs. Gibbs 40 and KW 55 exhibit a more rapid pressure increase with energy density compared to FSU2R, HPUC, and SINPA, indicating stiffer EOSs and thus higher sound speeds (figure 2). The right panel’s M-R relation shows that at lower masses, NSs have larger radii due to nuclear pressure counteracting gravity. As mass increases, gravitational forces dominate, reducing the radius until a maximum mass limit is reached, marked by

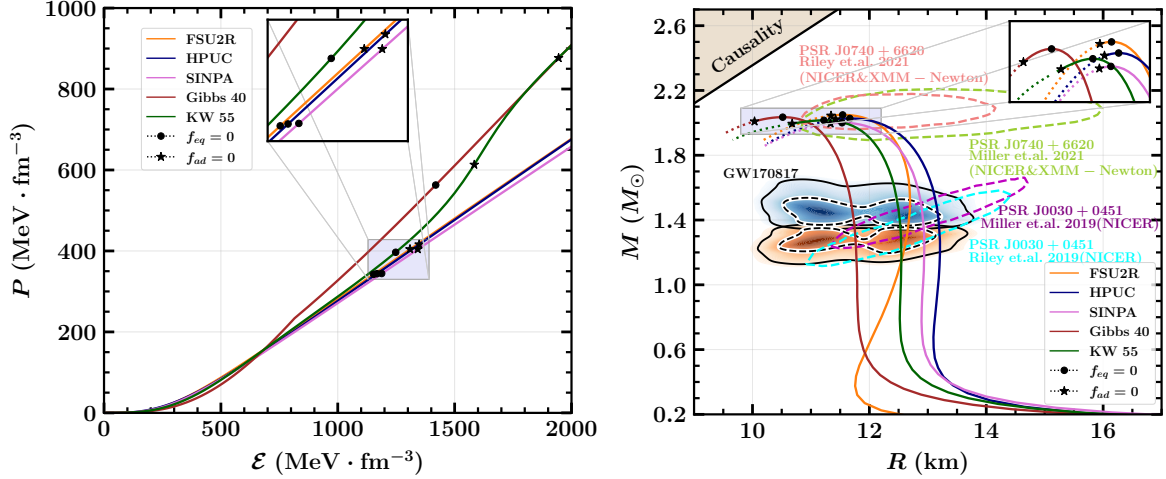


Figure 4. On the left panel EOSs are represented as pressure (P) versus energy density (ϵ). The composition of the three employed models is as follows: for FSU2R, HPUC & SINPA, nucleons and leptons; for Gibbs, nucleons, quarks, and leptons in a soft first-order phase transition description; and for KW, the same as for Gibbs, but in a cross-over description. The “zoomed plot” clearly shows the “dot” and “star” markers for hadronic EOSs. The right panel displays the Mass-Radius relationship obtained for our choice of EOSs. The astrophysical observable constraints on mass and radius from PSR J0740+6620 [15, 16], and NICER data for PSR J0030+0451 [81, 82] are represented by coloured regions. The outer and inner regions of the blue and orange butterfly structured plot indicate the 90% (solid) and 50% (dashed) confidence intervals based on the LIGO-Virgo analysis for Binary Neutron Star (BNS) components of the GW170817 event [83–85]. The “zoomed plot” clearly shows the stability regions (the region between the “dot” and “star” markers) for different EOS models. The “dotted” region after the “star” marker is the unstable region.

dot markers. Beyond this limit, NSs are unstable in the equilibrium case but may remain stable in the adiabatic case (star markers). Consequently, the adiabatic scenario allows NSs to exhibit smaller radii due to their higher compactness at the stability limit, as shown in table 3. This increased compactness shortens oscillation periods, leading to higher f -mode frequencies (table 2). The region between the dot and star markers, termed the “slow stable” region, indicates where NSs remain stable under adiabatic conditions despite slow responses to perturbations. Beyond the star markers (dotted portion), NSs collapse into black holes. The zoomed plot in the upper right corner of figure 4 highlights that the slow stable region is more extended for Gibbs 40 and KW 55 than for hadronic EOSs, consistent with the larger gap between equilibrium and adiabatic frequency vanishing points in figure 3.

5 Summary & conclusions

In this study, five distinct EOSs were analyzed, classified as hadronic (FSU2R, HPUC, SINPA) and hybrid (Gibbs 40, KW 55, with KW 55 featuring crossover matter), to explore their effects on neutron star (NS) properties. The investigation centres on how adiabatic scenarios, where particle composition remains fixed during compression, affect NS dynamical stability — a condition more applicable when reaction rates are slow. Adopting the adiabatic sound speed extends the stability region compared to the equilibrium case, creating a “slow stable”

region that persists only under slow reactions and becomes unstable if the composition adjusts to equilibrium rapidly.

Stability was evaluated by examining the fundamental radial f -mode oscillations, identifying the point of marginal stability where the frequency becomes zero. The marginal stability point in the adiabatic scenario extends beyond the maximum mass configuration, while that in the equilibrium scenario coincides with the maximum mass configuration. The region between these two marginal stability points corresponds to the intermediate slow stable region. For NSs of the same structure, the adiabatic f -mode frequency is higher than the equilibrium one, enabling the identification of stable and unstable regions on the mass-radius (M-R) curve. The adiabatic case supports greater compactness (as mass decreases, but radius decreases more, increasing compactness $C = M/R$) before the f -mode frequency drops to zero. For hadronic EOSs, the radius difference between equilibrium and adiabatic stability limits is about 0.2 km, while for Gibbs and KW EOSs, it is roughly 0.5 km, reflecting varying composition gradients. The difference is more pronounced in hybrid NSs than in hadronic NSs since the difference between adiabatic and equilibrium is greater in the former, which is a feature of additional quark degrees of freedom with steep quark composition gradient. The hybrid EOSs considered here feature either crossover phase transition or first-order phase transition under the Gibbs construction without density discontinuity. As a result, the radius difference is less than the 1 km difference observed with large density discontinuities [28, 34].

These results highlight the distinct effects of adiabatic and equilibrium sound speeds on NS radial oscillations and stability. In particular, the adiabatic scenario, which is more realistic under slow reaction rates, permits stability at greater compactness and smaller radii, allowing NSs to remain dynamically stable in configurations that would be unstable under equilibrium conditions. This extended stable branch implies that neutron stars can support higher compactness and reach lower radius before becoming unstable, potentially affecting radius measurements and interpretation of high-mass neutron stars. For instance, a radius below 11 km for a $2 M_\odot$ star might suggest it is on the “slow stable” branch, while PSR J0740+6620 ($R \approx 13$ km, $M = 2.08 \pm 0.07 M_\odot$) is likely on the regular stable branch, based on recent NICER observations [15, 16, 86, 87]. Our results demonstrate the need to account for both equilibrium and adiabatic conditions when evaluating radial oscillations and stability of NS. Although this stability analysis is based on linearized oscillations and small perturbations, larger oscillation displacements may be influenced by higher-order effects, as noted in previous studies [33].

Acknowledgments

B.K. acknowledges partial support from the Department of Science and Technology, Government of India, with grant no. CRG/2021/000101. TZ is supported by the Network for Neutrinos, Nuclear Astrophysics and Symmetries (N3AS), through the National Science Foundation Physics Frontier Center Grant No. PHY-2020275.

A Radial oscillation profile

In figure 5, we present the radial profiles of η_n and ζ_n for the f -mode ($n = 0$) and excited p-modes ($n = 1, 2$) in a $2 M_\odot$ neutron star under various EOSs. According to Sturm-Liouville

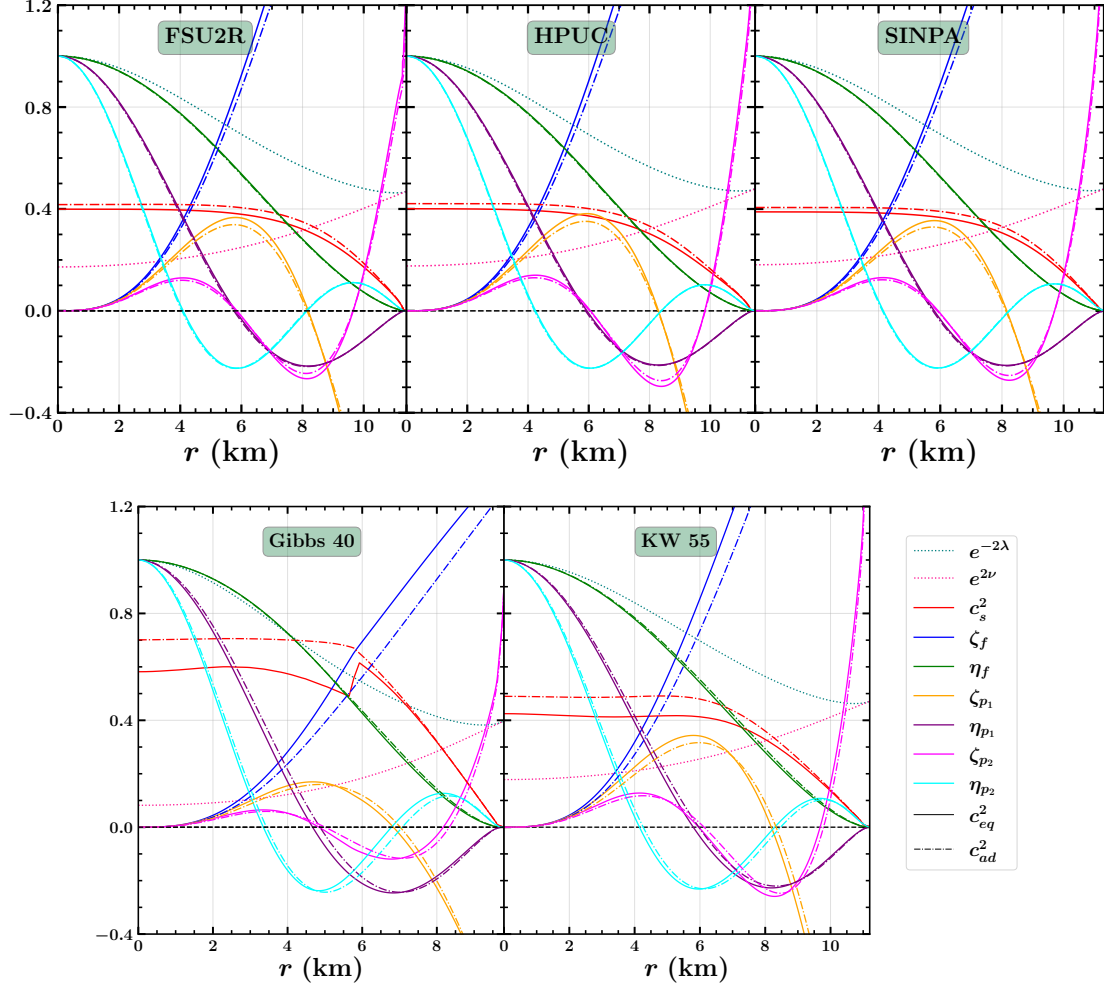


Figure 5. Radial profiles of ζ and η , for f -mode ($n = 0$) as well as two excited p -modes ($n = 1, 2$) in $2 M_\odot$ NS for FSU2R, HPUC, SINPA, Gibbs 40 and KW 55 EOSs. Also, we have shown the radial variation of two metric functions (λ & ν) and the sound speed square. All those variations are represented for equilibrium and adiabatic cases, shown by “solid” and “dash-dot” lines respectively.

theory, the eigenfunction ζ_n displays exactly n zeros (nodes) within the range $0 < r < R$. The function ζ_n , related to the radial displacement, and η_n , which represents the Lagrangian variation of pressure as $\eta = -\Delta P e^{\lambda+2\nu}$, both exhibit n zeros between the center and the stellar surface. As observed, ζ_n increases in amplitude with radial distance, while η_n oscillates with decreasing amplitude and eventually vanishes at the surface. The continuity of η_n and ΔP ensures that the system oscillates close to equilibrium [88]. For EOSs involving nucleonic matter ($npe\mu$), the radial profiles of ζ_n and η_n are smooth. However, in the Gibbs 40 EOS, we observe abrupt changes between 5.5 and 6 km, which is attributed to the onset of quark matter.

B Numerical results verification

To strengthen the validation of our numerical implementation, we have extended our analysis to include several additional EOSs beyond those discussed in the main text. Specifically,

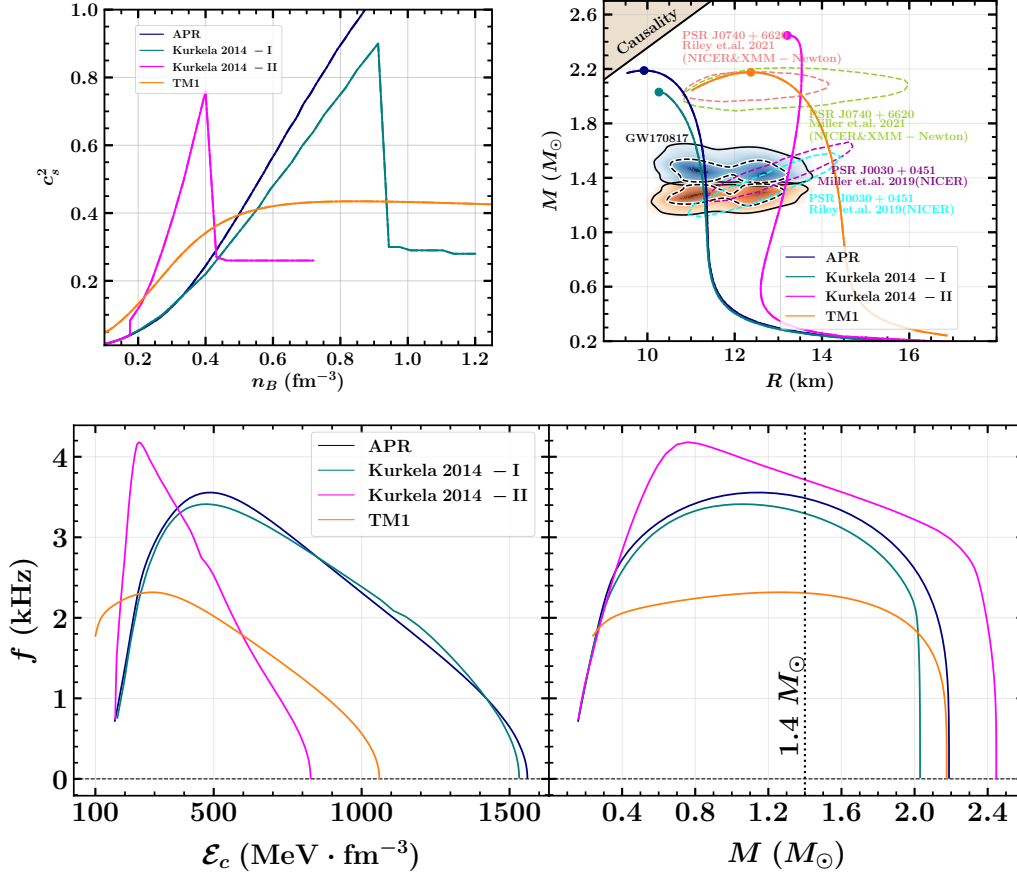


Figure 6. Upper panel: sound speed variation with baryon density and the Mass-Radius plot. Lower panel: f -mode frequency variation with central energy density and mass, for four different EOSs, APR [89], Kulkerla 2014-I & II [90] and TM1 [91], as shown in the referenced work, “Radial oscillations in neutron stars from QCD” [80].

we reproduce results from an independent study [80], which investigates radial oscillations in neutron stars using the APR [89], Kulkerla 2014-I & II [90], and TM1 [91] EOSs. Our computed f -mode frequencies are compared with those reported in that work, as shown in figure 6. The results exhibit close agreement across a wide range of central energy densities and stellar masses. Moreover, our code precisely reproduces the zero-crossing of the mode frequency at the maximum mass and central density values reported in the reference. This consistency confirms the accuracy of our Sturm-Liouville eigenvalue solver and supports its application to the EOSs considered in this study.

References

- [1] K.D. Kokkotas and B.G. Schmidt, *Quasinormal modes of stars and black holes*, *Living Rev. Rel.* **2** (1999) 2 [[gr-qc/9909058](#)] [[INSPIRE](#)].
- [2] J.L. Blázquez-Salcedo, F.S. Khoo, J. Kunz and V. Preut, *Polar Quasinormal Modes of Neutron Stars in Massive Scalar-Tensor Theories*, *Front. Phys.* **9** (2021) 741427 [[arXiv:2107.06726](#)] [[INSPIRE](#)].

- [3] H.-P. Nollert, *Quasinormal modes: the characteristic ‘sound’ of black holes and neutron stars*, *Class. Quant. Grav.* **16** (1999) R159 [INSPIRE].
- [4] E. Berti, V. Cardoso and A.O. Starinets, *Quasinormal modes of black holes and black branes*, *Class. Quant. Grav.* **26** (2009) 163001 [arXiv:0905.2975] [INSPIRE].
- [5] R.A. Konoplya and A. Zhidenko, *Quasinormal modes of black holes: From astrophysics to string theory*, *Rev. Mod. Phys.* **83** (2011) 793 [arXiv:1102.4014] [INSPIRE].
- [6] A. Passamonti, M. Bruni, L. Gualtieri, A. Nagar and C.F. Sopuerta, *Coupling of radial and axial non-radial oscillations of compact stars: Gravitational waves from first-order differential rotation*, *Phys. Rev. D* **73** (2006) 084010 [gr-qc/0601001] [INSPIRE].
- [7] A. Passamonti, N. Stergioulas and A. Nagar, *Gravitational Waves from Nonlinear Couplings of Radial and Polar Nonradial Modes in Relativistic Stars*, *Phys. Rev. D* **75** (2007) 084038 [gr-qc/0702099] [INSPIRE].
- [8] P. D’Avanzo, *Short gamma-ray bursts: A review*, *J. High Energy Astrophys.* **7** (2015) 73 [INSPIRE].
- [9] E. Berger, *Short-Duration Gamma-Ray Bursts*, *Ann. Rev. Astron. Astrophys.* **52** (2014) 43 [arXiv:1311.2603] [INSPIRE].
- [10] N. Jordana-Mitjans et al., *A Short Gamma-Ray Burst from a Protomagnetar Remnant*, *Astrophys. J.* **939** (2022) 106 [arXiv:2211.05810] [INSPIRE].
- [11] S. Dichiara et al., *Short gamma-ray bursts within 200 Mpc*, *Mon. Not. Roy. Astron. Soc.* **492** (2020) 5011 [arXiv:1912.08698] [INSPIRE].
- [12] C. Chirenti, M.C. Miller, T. Strohmayer and J. Camp, *Searching for hypermassive neutron stars with short gamma-ray bursts*, *Astrophys. J. Lett.* **884** (2019) L16 [arXiv:1906.09647] [INSPIRE].
- [13] J. Antoniadis et al., *A Massive Pulsar in a Compact Relativistic Binary*, *Science* **340** (2013) 6131 [arXiv:1304.6875] [INSPIRE].
- [14] H.T. Cromartie et al., *Relativistic Shapiro delay measurements of an extremely massive millisecond pulsar*, *Nat. Astron.* **4** (2020) 72 [arXiv:1904.06759] [INSPIRE].
- [15] M.C. Miller et al., *The Radius of PSR J0740+6620 from NICER and XMM-Newton Data*, *Astrophys. J. Lett.* **918** (2021) L28 [arXiv:2105.06979] [INSPIRE].
- [16] T.E. Riley et al., *A NICER View of the Massive Pulsar PSR J0740+6620 Informed by Radio Timing and XMM-Newton Spectroscopy*, *Astrophys. J. Lett.* **918** (2021) L27 [arXiv:2105.06980] [INSPIRE].
- [17] P. Ledoux and T. Walraven, *Variable Stars*, in *Encyclopedia of Physics* **11**, *Astrophysics II: Stellar Structure*, Springer (1958), pp. 353–604 [DOI:10.1007/978-3-642-45908-5_6].
- [18] S. Chandrasekhar, *Dynamical Instability of Gaseous Masses Approaching the Schwarzschild Limit in General Relativity*, *Phys. Rev. Lett.* **12** (1964) 114 [INSPIRE].
- [19] B.K. Harrison, K.S. Thorne, M. Wakano and J.A. Wheeler, *Gravitation Theory and Gravitational Collapse*, University of Chicago Press (1965).
- [20] J.M. Bardeen, K.S. Thorne and D.W. Meltzer, *A Catalogue of Methods for Studying the Normal Modes of Radial Pulsation of General-Relativistic Stellar Models*, *Astrophys. J.* **145** (1966) 505.
- [21] G. Chanmugam, *Radial oscillations of zero-temperature white dwarfs and neutron stars below nuclear densities*, *Astrophys. J.* **217** (1977) 799.

- [22] T. Zhao and J.M. Lattimer, *Quarkyonic Matter Equation of State in Beta-Equilibrium*, *Phys. Rev. D* **102** (2020) 023021 [[arXiv:2004.08293](#)] [[INSPIRE](#)].
- [23] D. Lai, *Resonant oscillations and tidal heating in coalescing binary neutron stars*, *Mon. Not. Roy. Astron. Soc.* **270** (1994) 611 [[astro-ph/9404062](#)] [[INSPIRE](#)].
- [24] P. Jaikumar, A. Sempowski, M. Prakash and C. Constantinou, *g-mode oscillations in hybrid stars: A tale of two sounds*, *Phys. Rev. D* **103** (2021) 123009 [[arXiv:2101.06349](#)] [[INSPIRE](#)].
- [25] C. Constantinou, T. Zhao, S. Han and M. Prakash, *Framework for phase transitions between the Maxwell and Gibbs constructions*, *Phys. Rev. D* **107** (2023) 074013 [[arXiv:2302.04289](#)] [[INSPIRE](#)].
- [26] J.P. Pereira, C.V. Flores and G. Lugones, *Phase transition effects on the dynamical stability of hybrid neutron stars*, *Astrophys. J.* **860** (2018) 12 [[arXiv:1706.09371](#)] [[INSPIRE](#)].
- [27] P.B. Rau and A. Sedrakian, *Two first-order phase transitions in hybrid compact stars: Higher-order multiplet stars, reaction modes, and intermediate conversion speeds*, *Phys. Rev. D* **107** (2023) 103042 [[arXiv:2212.09828](#)] [[INSPIRE](#)].
- [28] P.B. Rau and G.G. Salaben, *Nonequilibrium effects on stability of hybrid stars with first-order phase transitions*, *Phys. Rev. D* **108** (2023) 103035 [[arXiv:2309.08540](#)] [[INSPIRE](#)].
- [29] T. Zhao, C. Constantinou, P. Jaikumar and M. Prakash, *Quasinormal g modes of neutron stars with quarks*, *Phys. Rev. D* **105** (2022) 103025 [[arXiv:2202.01403](#)] [[INSPIRE](#)].
- [30] G. Lugones, M. Mariani and I.F. Ranea-Sandoval, *A model-agnostic analysis of hybrid stars with reactive interfaces*, *JCAP* **03** (2023) 028 [[arXiv:2106.10380](#)] [[INSPIRE](#)].
- [31] I.F. Ranea-Sandoval, M. Mariani, M.O. Celi, M.C. Rodríguez and L. Tonetto, *Asteroseismology using quadrupolar f-modes revisited: Breaking of universal relationships in the slow hadron-quark conversion scenario*, *Phys. Rev. D* **107** (2023) 123028 [[arXiv:2306.02823](#)] [[INSPIRE](#)].
- [32] V.P. Gonçalves and L. Lazzari, *Impact of slow conversions on hybrid stars with sequential QCD phase transitions*, *Eur. Phys. J. C* **82** (2022) 288 [[arXiv:2201.03304](#)] [[INSPIRE](#)].
- [33] E. Gourgoulhon, P. Haensel and D. Gondek, *Maximum mass instability of neutron stars and weak interaction processes in dense matter*, *Astron. Astrophys.* **294** (1995) 747.
- [34] I.A. Rather, K.D. Marquez, B.C. Backes, G. Panotopoulos and I. Lopes, *Radial oscillations of hybrid stars and neutron stars including delta baryons: the effect of a slow quark phase transition*, *JCAP* **05** (2024) 130 [[arXiv:2401.07789](#)] [[INSPIRE](#)].
- [35] M. Mariani, I.F. Ranea-Sandoval, G. Lugones and M.G. Orsaria, *Could a slow stable hybrid star explain the central compact object in HESS J1731-347?*, *Phys. Rev. D* **110** (2024) 043026 [[arXiv:2407.06347](#)] [[INSPIRE](#)].
- [36] S. Sen et al., *Radial Oscillations in Neutron Stars from Unified Hadronic and Quarkyonic Equation of States*, *Galaxies* **11** (2023) 60 [[arXiv:2205.02076](#)] [[INSPIRE](#)].
- [37] P. Routaray, H.C. Das, S. Sen, B. Kumar, G. Panotopoulos and T. Zhao, *Radial oscillations of dark matter admixed neutron stars*, *Phys. Rev. D* **107** (2023) 103039 [[arXiv:2211.12808](#)] [[INSPIRE](#)].
- [38] S.R. Mohanty, S. Ghosh and B. Kumar, *Unstable anisotropic neutron stars: Probing the limits of gravitational collapse*, *Phys. Rev. D* **109** (2024) 123039 [[arXiv:2304.02439](#)] [[INSPIRE](#)].
- [39] L. Tolos, M. Centelles and A. Ramos, *Equation of State for Nucleonic and Hyperonic Neutron Stars with Mass and Radius Constraints*, *Astrophys. J.* **834** (2017) 3 [[arXiv:1610.00919](#)] [[INSPIRE](#)].

- [40] A. Sharma, M. Kumar, S. Kumar, V. Thakur, R. Kumar and S.K. Dhiman, *New equations of state for dense nuclear matter properties*, *Nucl. Phys. A* **1040** (2023) 122762 [[INSPIRE](#)].
- [41] C. Mondal, B.K. Agrawal, J.N. De and S.K. Samaddar, *Sensitivity of elements of the symmetry energy of nuclear matter to the properties of neutron-rich systems*, *Phys. Rev. C* **93** (2016) 044328 [[arXiv:1603.08645](#)] [[INSPIRE](#)].
- [42] R.O. Gomes, P. Char and S. Schramm, *Constraining strangeness in dense matter with GW170817*, *Astrophys. J.* **877** (2019) 139 [[arXiv:1806.04763](#)] [[INSPIRE](#)].
- [43] T. Klähn and T. Fischer, *Vector interaction enhanced bag model for astrophysical applications*, *Astrophys. J.* **810** (2015) 134 [[arXiv:1503.07442](#)] [[INSPIRE](#)].
- [44] N.K. Glendenning, *First order phase transitions with more than one conserved charge: Consequences for neutron stars*, *Phys. Rev. D* **46** (1992) 1274 [[INSPIRE](#)].
- [45] N.K. Glendenning, *Phase transitions and crystalline structures in neutron star cores*, *Phys. Rep.* **342** (2001) 393 [[INSPIRE](#)].
- [46] J.I. Kapusta and T. Welle, *Neutron stars with a crossover equation of state*, *Phys. Rev. C* **104** (2021) L012801 [[arXiv:2103.16633](#)] [[INSPIRE](#)].
- [47] C. Constantinou, S. Han, P. Jaikumar and M. Prakash, *g modes of neutron stars with hadron-to-quark crossover transitions*, *Phys. Rev. D* **104** (2021) 123032 [[arXiv:2109.14091](#)] [[INSPIRE](#)].
- [48] H. Müller and B.D. Serot, *Relativistic mean field theory and the high density nuclear equation of state*, *Nucl. Phys. A* **606** (1996) 508 [[nucl-th/9603037](#)] [[INSPIRE](#)].
- [49] M. Del Estal, M. Centelles, X. Viñas and S.K. Patra, *Pairing properties in relativistic mean field models obtained from effective field theory*, *Phys. Rev. C* **63** (2001) 044321 [[nucl-th/0101065](#)] [[INSPIRE](#)].
- [50] R.J. Furnstahl, B.D. Serot and H.-B. Tang, *A Chiral effective Lagrangian for nuclei*, *Nucl. Phys. A* **615** (1997) 441 [[nucl-th/9608035](#)] [[INSPIRE](#)].
- [51] S.K. Singh, M. Bhuyan, P.K. Panda and S.K. Patra, *The effect of isoscalar-isovector coupling in infinite nuclear matter*, *J. Phys. G* **40** (2013) 085104 [[arXiv:1211.5461](#)] [[INSPIRE](#)].
- [52] B. Kumar, S. Singh, B. Agrawal and S. Patra, *New parameterization of the effective field theory motivated relativistic mean field model*, *Nucl. Phys. A* **966** (2017) 197 [[arXiv:1705.02621](#)] [[INSPIRE](#)].
- [53] B. Kumar, S.K. Patra and B.K. Agrawal, *New relativistic effective interaction for finite nuclei, infinite nuclear matter and neutron stars*, *Phys. Rev. C* **97** (2018) 045806 [[arXiv:1711.04940](#)] [[INSPIRE](#)].
- [54] A. Kumar, H.C. Das, S.K. Biswal, B. Kumar and S.K. Patra, *Warm dense matter and cooling of supernovae remnants*, *Eur. Phys. J. C* **80** (2020) 775 [[arXiv:2005.08320](#)] [[INSPIRE](#)].
- [55] H.C. Das, A. Kumar, B. Kumar et al., *Effects of dark matter on the nuclear and neutron star matter*, *Mon. Not. Roy. Astron. Soc.* **495** (2020) 4893 [[arXiv:2002.00594](#)] [[INSPIRE](#)].
- [56] P. Routaray et al., *Investigating dark matter-admixed neutron stars with NITR equation of state in light of PSR J0952-0607*, *JCAP* **10** (2023) 073 [[arXiv:2304.05100](#)] [[INSPIRE](#)].
- [57] R. Furnstahl, B.D. Serot and H.-B. Tang, *Analysis of chiral mean field models for nuclei*, *Nucl. Phys. A* **598** (1996) 539 [[nucl-th/9511028](#)] [[INSPIRE](#)].
- [58] S.K. Singh, S.K. Biswal, M. Bhuyan and S.K. Patra, *Effect of isospin asymmetry in a nuclear system*, *J. Phys. G* **41** (2014) 055201 [[arXiv:1310.5689](#)] [[INSPIRE](#)].

- [59] N.K. Glendenning, *Neutron Stars Are Giant Hypernuclei?*, *Astrophys. J.* **293** (1985) 470 [INSPIRE].
- [60] P.G. Reinhard, *The nonlinearity of the scalar field in a relativistic mean-field theory of the nucleus*, *Z. Phys. A* **329** (1988) 257 [INSPIRE].
- [61] V. Tran, S. Ghosh, N. Lozano, D. Chatterjee and P. Jaikumar, *g-mode oscillations in neutron stars with hyperons*, *Phys. Rev. C* **108** (2023) 015803 [arXiv:2212.09875] [INSPIRE].
- [62] H.A. Bethe, *Theory of nuclear matter*, *Annu. Rev. Nucl. Part. Sci.* **21** (1971) 93 [INSPIRE].
- [63] G. Colò, U. Garg and H. Sagawa, *Symmetry energy from the nuclear collective motion: constraints from dipole, quadrupole, monopole and spin-dipole resonances*, *Eur. Phys. J. A* **50** (2014) 26 [arXiv:1309.1572] [INSPIRE].
- [64] P. Danielewicz and J. Lee, *Symmetry Energy II: Isobaric Analog States*, *Nucl. Phys. A* **922** (2014) 1 [arXiv:1307.4130] [INSPIRE].
- [65] L. Brandes, W. Weise and N. Kaiser, *Inference of the sound speed and related properties of neutron stars*, *Phys. Rev. D* **107** (2023) 014011 [arXiv:2208.03026] [INSPIRE].
- [66] C. Ecker and L. Rezzolla, *A General, Scale-independent Description of the Sound Speed in Neutron Stars*, *Astrophys. J. Lett.* **939** (2022) L35 [arXiv:2207.04417] [INSPIRE].
- [67] S. Chatterjee, H. Sudhakaran and R. Mallick, *Analyzing the speed of sound in neutron star with machine learning*, *Eur. Phys. J. C* **84** (2024) 1291 [arXiv:2302.13648] [INSPIRE].
- [68] B. Reed and C.J. Horowitz, *Large sound speed in dense matter and the deformability of neutron stars*, *Phys. Rev. C* **101** (2020) 045803 [arXiv:1910.05463] [INSPIRE].
- [69] S. Altiparmak, C. Ecker and L. Rezzolla, *On the Sound Speed in Neutron Stars*, *Astrophys. J. Lett.* **939** (2022) L34 [arXiv:2203.14974] [INSPIRE].
- [70] P. Bedaque and A.W. Steiner, *Sound velocity bound and neutron stars*, *Phys. Rev. Lett.* **114** (2015) 031103 [arXiv:1408.5116] [INSPIRE].
- [71] E. Ferrer and A. Hackebill, *Speed of sound for hadronic and quark phases in a magnetic field*, *Nucl. Phys. A* **1031** (2023) 122608 [arXiv:2203.16576] [INSPIRE].
- [72] N. Yao, A. Sorensen, V. Dexheimer and J. Noronha-Hostler, *Structure in the speed of sound: From neutron stars to heavy-ion collisions*, *Phys. Rev. C* **109** (2024) 065803 [arXiv:2311.18819] [INSPIRE].
- [73] G. Hoyer, *Oscillations in Neutron Stars*, Ph.D. Thesis, University of Cambridge (1986).
- [74] L. Landau and E. Lifshitz, *The Classical Theory of Fields*, Butterworth-Heinemann (1967).
- [75] J.R. Oppenheimer and G.M. Volkoff, *On massive neutron cores*, *Phys. Rev.* **55** (1939) 374 [INSPIRE].
- [76] R.C. Tolman, *Static solutions of Einstein's field equations for spheres of fluid*, *Phys. Rev.* **55** (1939) 364 [INSPIRE].
- [77] K.D. Kokkotas and J. Ruoff, *Radial oscillations of relativistic stars*, *Astron. Astrophys.* **366** (2001) 565 [gr-qc/0011093] [INSPIRE].
- [78] J. Hladík, C. Posada and Z. Stuchlík, *Radial instability of trapping polytropic spheres*, *Int. J. Mod. Phys. D* **29** (2020) 2050030 [arXiv:2001.05999] [INSPIRE].
- [79] P. Routaray, A. Quddus, K. Chakravarti and B. Kumar, *Probing the impact of WIMP dark matter on universal relations, GW170817 posterior, and radial oscillations*, *Mon. Not. Roy. Astron. Soc.* **525** (2023) 5492 [arXiv:2202.04364] [INSPIRE].

- [80] J.C. Jiménez and E.S. Fraga, *Radial oscillations in neutron stars from QCD*, *Phys. Rev. D* **104** (2021) 014002 [[arXiv:2104.13480](#)] [[INSPIRE](#)].
- [81] M.C. Miller et al., *PSR J0030+0451 Mass and Radius from NICER Data and Implications for the Properties of Neutron Star Matter*, *Astrophys. J. Lett.* **887** (2019) L24 [[arXiv:1912.05705](#)] [[INSPIRE](#)].
- [82] T.E. Riley et al., *A NICER View of PSR J0030+0451: Millisecond Pulsar Parameter Estimation*, *Astrophys. J. Lett.* **887** (2019) L21 [[arXiv:1912.05702](#)] [[INSPIRE](#)].
- [83] LIGO SCIENTIFIC and VIRGO collaborations, *GW170817: Observation of Gravitational Waves from a Binary Neutron Star Inspiral*, *Phys. Rev. Lett.* **119** (2017) 161101 [[arXiv:1710.05832](#)] [[INSPIRE](#)].
- [84] F.J. Fattoyev, J. Piekarewicz and C.J. Horowitz, *Neutron Skins and Neutron Stars in the Multimessenger Era*, *Phys. Rev. Lett.* **120** (2018) 172702 [[arXiv:1711.06615](#)] [[INSPIRE](#)].
- [85] N.K. Patra, A. Venneti, S.M.A. Imam, A. Mukherjee and B.K. Agrawal, *Systematic analysis of the impacts of symmetry energy parameters on neutron star properties*, *Phys. Rev. C* **107** (2023) 055804 [[arXiv:2302.03906](#)] [[INSPIRE](#)].
- [86] T. Salmi et al., *The Radius of the High-mass Pulsar PSR J0740+6620 with 3.6 yr of NICER Data*, *Astrophys. J.* **974** (2024) 294 [[arXiv:2406.14466](#)] [[INSPIRE](#)].
- [87] A.J. Dittmann et al., *A More Precise Measurement of the Radius of PSR J0740+6620 Using Updated NICER Data*, *Astrophys. J.* **974** (2024) 295 [[arXiv:2406.14467](#)] [[INSPIRE](#)].
- [88] F. Di Clemente, M. Mannarelli and F. Tonelli, *Reliable description of the radial oscillations of compact stars*, *Phys. Rev. D* **101** (2020) 103003 [[arXiv:2002.09483](#)] [[INSPIRE](#)].
- [89] A. Akmal, V.R. Pandharipande and D.G. Ravenhall, *The Equation of state of nucleon matter and neutron star structure*, *Phys. Rev. C* **58** (1998) 1804 [[nucl-th/9804027](#)] [[INSPIRE](#)].
- [90] A. Kurkela, E.S. Fraga, J. Schaffner-Bielich and A. Vuorinen, *Constraining neutron star matter with Quantum Chromodynamics*, *Astrophys. J.* **789** (2014) 127 [[arXiv:1402.6618](#)] [[INSPIRE](#)].
- [91] H. Shen, H. Toki, K. Oyamatsu and K. Sumiyoshi, *Relativistic equation of state of nuclear matter for supernova and neutron star*, *Nucl. Phys. A* **637** (1998) 435 [[nucl-th/9805035](#)] [[INSPIRE](#)].